ASME Letters in Dynamic Systems and Control
Online journal at:
https://asmedigitalcollection.asme.org/lettersdynsys

Aleksandr Shkoruta
Department of Mechanical Engineering,
Rensselaer Polytechnic Institute,
110 8th Street,
Troy, NY 12180
e-mail: shkora@rpi.edu

Bumsoo Park[1]
Department of Mechanical Engineering,
Rensselaer Polytechnic Institute,
110 8th Street,
Troy, NY 12180
e-mail: parkb5@rpi.edu

Sandipan Mishra
Department of Mechanical Engineering,
Rensselaer Polytechnic Institute,
110 8th Street,
Troy, NY 12180
e-mail: mishrs2@rpi.edu

An Empirical Model and Feedforward Control of Laser Powder Bed Fusion

Reliable process control for the laser powder bed fusion process, especially at the melt pool scale, remains an open challenge. One of the reasons for this is the lack of suitable control-oriented models and associated control design strategies. To address this issue, this paper (1) identifies an empirical control-oriented model of geometry-dependent melt pool behavior and (2) experimentally demonstrates melt pool regulation with a feedforward controller for laser power based on this model. First, the study establishes that the melt pool signature increases as the scan lines decrease in length. An empirical model of this behavior is developed and validated on different geometries at varying laser power levels. Second, the model is used to design a line-to-line feedforward controller that provides an optimal laser power sequence for a given geometry. Finally, this controller is validated experimentally and is demonstrated to suppress the in-layer geometry-related melt pool signal deviations for different test geometries. [DOI: 10.1115/1.4064171]

Keywords: laser powder bed fusion, data-driven control, model-based feedforward, dynamics and control, manufacturing systems, modeling

1 Introduction

Quality control of the laser powder bed fusion (LPBF) parts remains an open research problem, as LPBF parts are prone to defects such as cracks, porosity [1], and poor surface finish [2,3]. Since LPBF part quality is strongly related to melt pool behavior [4], the regulation of melt pool geometry through laser power control is of particular interest. The laser power control problem can be cast as a melt pool regulation problem: the goal is to design the laser power profile to compensate for deviations in the melt pool temperature or geometry, ultimately reducing such effects as dross formation or overheating, e.g., in acute corners.

Prior research has shown that the melt pool can be regulated with a feedback controller based on measurements from a photodiode [5,6] or a camera [7–9] signal. However, feedback control in LPBF is challenging due to the high demands on the controller response time and the need for additional sensor-in-the-loop synchronization. Thus, the majority of existing literature focuses on the investigation of feedforward control strategies. Some of these strategies are model-free, such as the layer-to-layer data-driven control developed in Ref. [10] and the adjustment of the laser power based on geometry- and residual heat-based heuristics [11,12]. Others employ purely data-driven models: Yeung et al. [13] developed a regression model for melt pool size, while Ren and Wang [14] modeled the dynamics as a Gaussian process. The disadvantage of purely data-driven models is that they do not readily support control design strategies and are difficult to interpret. On the other hand, finite element process models are computationally expensive [4] and are poorly suited for process control. Recently, several reduced-order models have been reported in the literature [15,16], though no experimental validation was provided therein. A good example of an interpretable, control-oriented model of the melt pool behavior with experimental validation is presented in Ref. [17], where a model-based feedforward control application was demonstrated on a single-track scale. Thus, there is a lack of (a) interpretable, control-oriented models for melt pool in LPBF and (b) experimental application thereof on a *part scale*. From a physical understanding of LPBF, it is reasonable to expect that geometric features of the scan layer, i.e., sharp corners or narrow areas, can affect the melt pool behavior: if the laser quickly returns in proximity to the scanned point, it is likely that residual heat will not have dissipated completely. As a result, the melt pool increases in size at these locations, ultimately causing variability in the melt pool geometry. Currently, such melt pool variation issues are primarily addressed through a priori manual process parameter optimization. To address these gaps in current control design efforts in LPBF, this work focuses on (a) the development of a geometry-aware control-oriented model of the melt pool behavior and (b) the experimental implementation of feedforward control for LPBF based on this model.

The primary contributions of this work are the following:

(1) Repeatable geometry-determined deviations of melt pool signatures (related to the decreasing scan line lengths) are reported. A control-oriented process model of these geometry-related deviations is identified from empirical data and experimentally validated. The model is shown to be applicable to different scanning geometries and scan patterns (Sec. 4).
(2) A model-based feedforward controller is designed to suppress these deviations. The control problem is formulated as an optimization problem for laser power that varies line

[1]Corresponding author.
Manuscript received July 31, 2023; final manuscript received November 9, 2023; published online January 2, 2024. Assoc. Editor: Zhen Zhang.

by line. The process output is predicted by the identified empirical model (Sec. 5.1).

(3) The controller output is validated experimentally through builds of test parts. The experimental application of the designed controller on a part scale decreased geometric deviations in melt pool signal by 50% for different part geometries (Sec. 5.2).

2 Problem Formulation

As will be shown in Sec. 4, the geometry-dependent behavior of the melt pool can be modeled, given the laser power and the geometry of the scan pattern, i.e., the length of the nearby scan lines. Thus, the observed geometry-dependent measurement of the melt pool can be modeled, line by line, from empirical data, as function $M(p_n, p_{n-1}, l_n, l_{n-1})$, where p_n is the laser power, commanded while scanning line n, and l_n is the length of that line, while p_{n-1} and l_{n-1} correspond to the previous scan line (Fig. 1).

The goal is then to regulate this varying melt pool signal to a constant level by adjusting the laser power on a line-by-line basis. Given the identified model M, the problem can be formulated as a minimization of the difference between the observed signal and a reference:

$$P^* = \arg\min_{\tilde{P}} \sum_{n=0}^{L} \|M(p_n, l_n) - y_{ref}\|^2$$
$$\text{s.t. } p_n \le p_{\max}, \quad p_n \ge p_{\min} \forall n \tag{1}$$

where $n = 0, 1, \ldots, L$ is an index of a scan line, L is the total number of lines within a layer, l_n is the length of the nth scan line, p_n is the power value for the nth line, $\tilde{P} \triangleq [p_0, p_1, \ldots, p_L]$ is a vector of line-by-line laser powers, and y_{ref} is the desired level of the observed melt pool measurement. Search for the solution of Eq. (1) is subject to lower ($p_{\min}$) and upper ($p_{\max}$) power limits for safety reasons. As the scanning pattern $\{l_n\}$, $n = 0, 1, \ldots, L$ is known a priori, the solution P^* can be computed in advance and implemented in a feedforward controller, as discussed in Sec. 5.

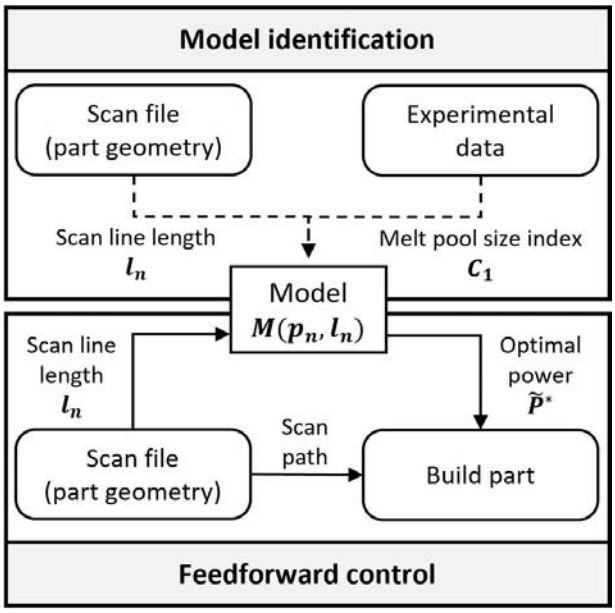

Fig. 1 Model identification and feedforward control for LPBF. The goal is to find a model that accurately represents geometry-related behavior in the measurements on a line-by-line basis and to derive the optimal power profile through the identified model. *n* denotes the line index.

3 Experimental Setup

3.1 Hardware and Instrumentation. This research was performed on an open-architecture LPBF machine described in Ref. [10]. The machine is equipped with a SCANLAB intelli*SCAN*$_{\text{de}}$20 galvoscanner and a 400 W NdYAG laser and can build parts up to 50×50 mm^2 in cross section from commercially available metal powders, e.g., stainless steel. The supervisory control of the machine is achieved via AMERICA MAKES software [18], augmented with in-house developed C++ code. The low-level control of the scanning process, i.e., laser positioning and firing, is handled by the scanner control board. The scanning instructions for a layer are formatted as a text file containing a list of straight lines (scan file). Each line in the scan file is defined by start and end points, a laser power level, and a scanning speed value. Thus, the machine allows adjustment of the laser power within a layer on a line-by-line basis simply by modifying the input scan file.

To monitor the melt pool during the LPBF process, a coaxial camera-based setup, similar to that described in the literature [5,19,20], is integrated with the LPBF testbed. A Basler acA2000-165umNIR camera acquires 8-bit intensity images in the near-infrared band (800–950 nm) by looking at the melt pool through laser scanning optics. Each image is 64×64 pixels in size, with an instantaneous field of view of 22 μm per pixel. The camera acquires 2000 frames per second. A typical melt pool image (post-processed in MATLAB is shown in Fig. 2.

3.2 Image Data Processing. In this work, a unidimensional melt pool signature indicative of the melt pool size, is extracted from an image, enabling a single input single output (SISO) representation. One way to reduce the image dimensionality is to study the dimensions of its "features," e.g., the area of a large low-intensity "droplet" of a near-zero emission intensity or a small but bright "hot spot" in the center, as shown in Fig. 2. Such "features" can be quantified by the following signals:

$$C_\alpha = \sum_{r,c} 1[I(r, c) \ge \alpha] \tag{2}$$

where r, c are row and column pixel coordinates, $I(r, c)$ is an image intensity of the pixel at (r, c), α is a threshold, and $1[\ldots]$ stands for the indicator function, e.g., it is equal to 1 when its argument is true and is 0 otherwise. Specifically for the "droplet," or the total footprint of the melt pool emission, an area of the level set at low threshold $\alpha = 1$ is appropriate, i.e., C_1 (count of non-zero pixels) is an appropriate measurement to describe the total melt pool footprint.

The melt pool location on the build plate at a given point in time was determined based on the nominal scan pattern, assuming constant scanning velocity and perfect trajectory tracking by the galvoscanner. Given the camera-assigned time stamp and the positional commands that define the layer scanning sequence, the 1D melt pool signature, such as C_1, can be transformed from a time series

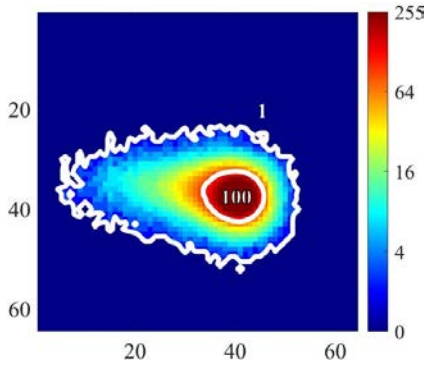

Fig. 2 Typical melt pool image (false color, logarithmic scale of intensity). Level sets at $\alpha = 1$ and $\alpha = 100$ are highlighted in white.

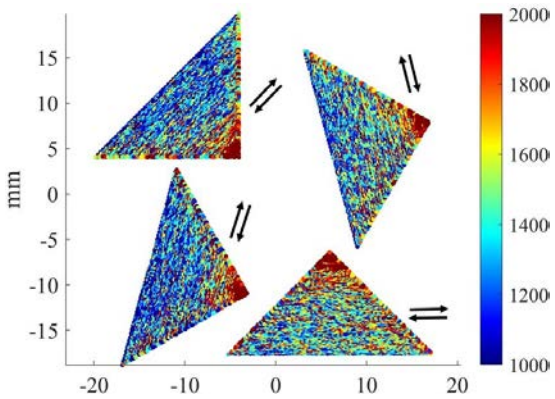

Fig. 3 Example of C_1, in pixels, as mapped to the nominal scanning position (x, y) on the build plate, for a build layer. Arrows indicate scanning direction for each part.

$C_1(t)$ to a spatial map $C_1(x, y)$ and plotted as a function of spatial coordinates in 2D, as illustrated in Fig. 3.

Remark. At length scales below 500 μm, the mapping of the nominal scan pattern to a measurement is imprecise due to the lack of positional feedback. Thus, in this work, images belonging to a line shorter than 0.5 mm were excluded from the model identification.

4 Model Identification

4.1 Model Structure. A prismatic part in Fig. 4 was designed to investigate if a quick return of the laser in the proximity of the previously scanned track would influence the melt pool behavior. The part consists of four stacked prisms $G1$–$G4$, triangular in cross section. There are four orientations of the scanning raster pattern throughout the part (i.e., four different hatch angles $S1$–$S4$). The whole build included four parts ($P1$–$P4$) of the same geometry. This way, a large variety of corner scan patterns, with repetition, could be studied: 174 layers were built for each part $P1$–$P4$, with each scan pattern $S1$–$S4$ repeating at least 10 times. Process parameters were set as follows: laser power 225 W, scanning velocity 800 mm/s, hatch spacing 90 μm, and continuous meander (snake-like) linear scan pattern. This test will be referred to as the *TP* (triangle prism) test.

The coaxial images acquired from the *TP* repeatedly showed geometry-dependent behavior: C_1 would raise in a corner, if the laser was scanning "into" it. The C_1 was found to exponentially depend on the length of the scan line (Fig. 5), i.e., $C_1 = a + b\exp(-l)$, where l is the scan line length. The effect was independent of the orientation of the scan pattern, the orientation of the part within the process chamber, the corner angle, or the areal size of the triangle.

4.2 Model Parameterization by Laser Power. To investigate the dependence of model parameters on input laser power, four different laser powers (150 W, 175 W, 200 W, and 225 W) were used to build eight cubes, with each power replicating twice. Each cube was scanned at three different angles: 30 deg , 135 deg, and 60 deg (Fig. 6). The hatch spacing, scanning velocity, and meander scan were repeated from the *TP* test. This test is referred to as *Cubes* in the following text.

The exponential behavior for C_1 persisted with all four laser powers. The experimental data were split in such a way that there were 12 equal subsets, six layers each, for each laser power, with

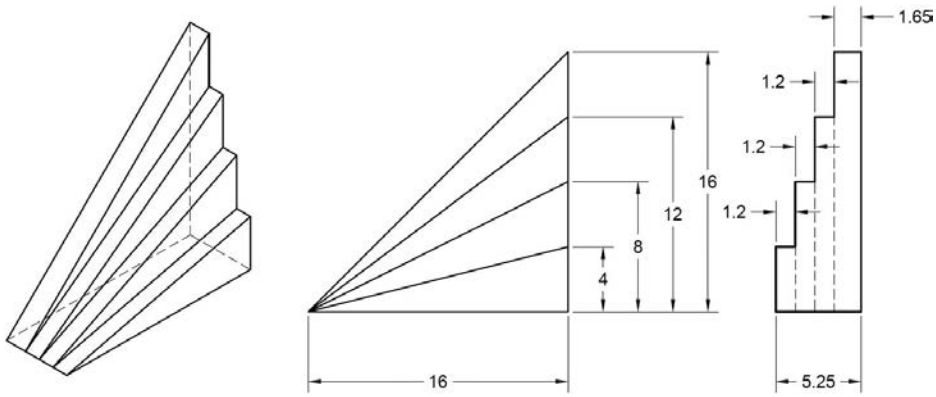

Fig. 4 Triangle prism for *TP* test

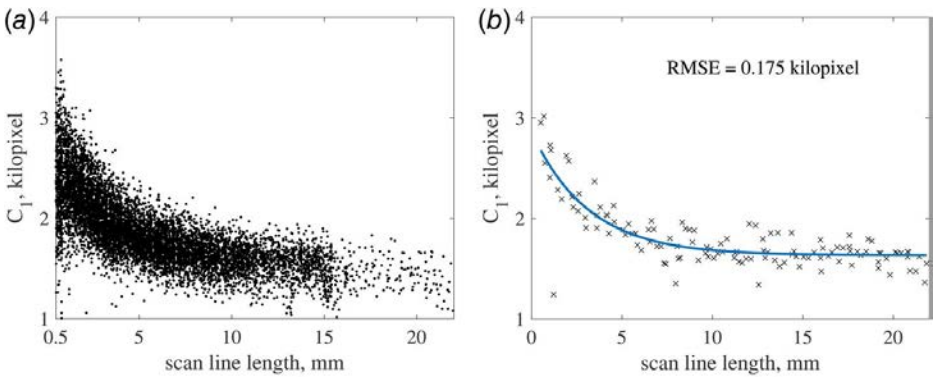

Fig. 5 (*a*) Measurements of C_1 from different P, G, and S combinations plotted against scan line length. A clear exponential trend is observed and (*b*) Exponential model as fitted to one scan P4, G1, and S1.

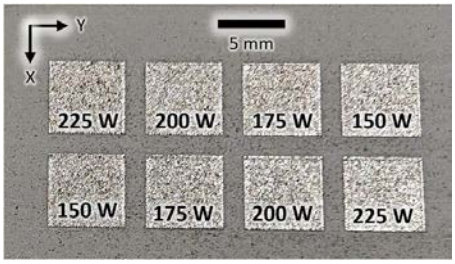

Fig. 6 Cubes test for model identification. Varying power values with three scan directions (30 deg, 135 deg, and 60 deg) were used.

three build layers reserved for model validation. Figure 7 illustrates different models that were identified from the data. Evidently, the parameters of the exponential model can be parameterized with the laser power; therefore, a *single-line* model of C_1 is as follows:

$$M_s(p) = C_\infty(p) + \Delta C(p) \exp\left(-l/r(p)\right) \tag{3}$$

where l is the scan line length, and $C_\infty(p)$, $\Delta C(p)$, and $r(p)$ are the functions found from the *Cubes* dataset:

$$\begin{aligned} C_\infty(p) &= 10.6p - 880 \\ \Delta C(p) &= -0.12p^2 + 41p - 2268 \\ r(p) &= 0.03p \end{aligned} \tag{4}$$

Figure 8 illustrates the model fit to one of the validation layers from *Cubes*. The coaxial signal C_1 exhibits high variation; thus, a filtered signal had to be used to quantify the geometry-related trend and the model's fit to it. It appears that the identified model captured the in-layer signal trend well.

4.3 Control-Oriented Model. The model above captures the effect of scan length and laser power on the C_1 measurements for a given line when the laser power is constant throughout a part. The question is: once the laser power starts changing from one line to the next, how should the model change? The first term $C_\infty(p)$ can be interpreted as a steady-state output corresponding to a specific power. The dynamic effect of the scan pattern is limited to the second term, and it might be interpreted as the contribution of the *previous* scanning to the C_1. Therefore, the exponential term should receive the values of laser power and scan line length from the *previous* line, which yields

$$M_c(p, n) = C_\infty(p_n) + \Delta C(p_{n-1}) e^{-\frac{l_{n-1}}{r(p_{n-1})}} \tag{5}$$

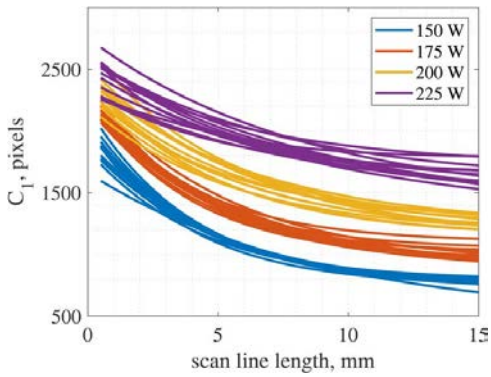

Fig. 7 The dependence of the exponential fit on laser power. There are 12 fits for each laser power.

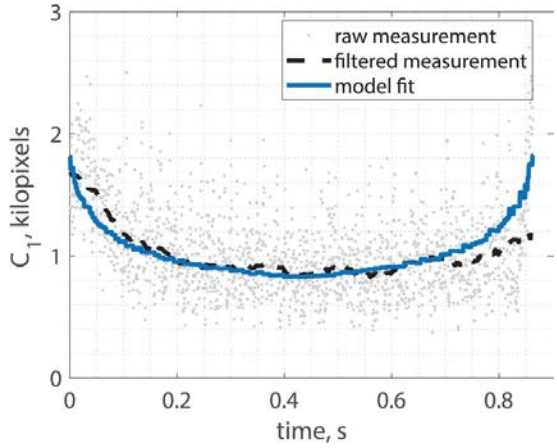

Fig. 8 Illustration of the model fit on the validation data. One out of 24 validation layers shown. Notice the high variation of the raw measurement. However, general trend (higher signal in the corners, at the beginning and at the end of the scan) is captured well. To extract the trend, median filter *F* with the window size of 150 samples was used.

where n is the line index in the scan sequence. For continuous scan patterns, subsequent scan lines do not change rapidly, and the approximation of $l_n \approx l_{n-1}$ is reasonable. The functions $C_\infty(p)$, $\Delta C(p)$, and $r(p)$ remain the same as in Eq. (4).

5 Model-Based Feedforward Control

For the in situ demonstration of the feedforward control, two additional geometries were used. The *Star* and *Wave* geometries are shown in Fig. 9. They were designed with curved edges to distinguish them from the simple shapes of *TP* and *Cubes* to further support the efficacy of the proposed controller. *Star* was scanned at 0 deg and 90 deg (horizontally and vertically), while *Wave* was scanned at three different angles (cycling through 0 deg, 45 deg, 0 deg, and 135 deg). The nominal laser power was set to 200 W, while the scanning speed and hatch spacing remained the same as in other tests.

5.1 Controller Design. The control problem, as discussed in Sec. 2, is to find the optimal vector of line-by-line powers $\tilde{P} \triangleq [p_0, p_1, \ldots, p_L]$, such that the difference between all values of $C_1(n)$ and the reference C_{ref} is minimized over the whole layer, on a line-by-line basis, subject to lower and upper power limits.

Given the model (5) and scan pattern geometries, the optimal line-by-line power profiles were found for the *Star* and *Wave* parts, via MATLAB with the fmincon function, for all unique scan patterns of these two geometries. Power limits were defined as 150 W and 225 W, and the desired level for C_1 was set to $C_{\text{ref}} = 1500$ (the average observed value of C_1 in open-loop tests).

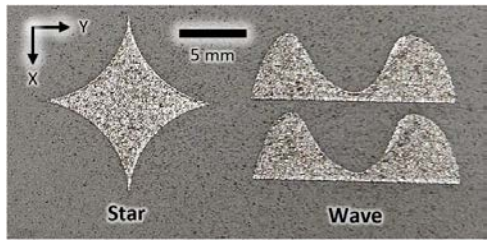

Fig. 9 Build parts for experimental validation of the control-oriented model: *Star* and *Wave*

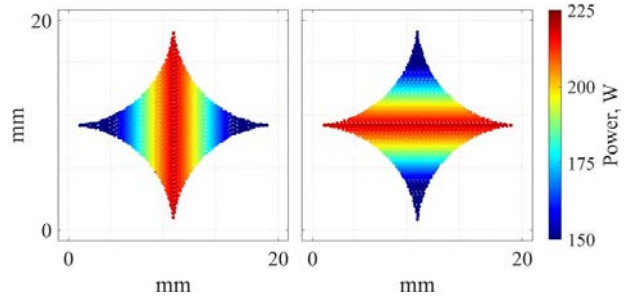

Fig. 10 Optimal power profiles for *Star* geometry. Horizontal and vertical scans are identical up to the rotation due to the part symmetry.

The optimized laser power profiles are shown in Figs. 10 and 11. These power profiles, once applied in situ, should have reduced or completely eliminated the geometry-dependent behavior of the coaxial signature C_1.

5.2 Experimental Validation. The optimized power profiles were subsequently tested experimentally. Each of the layer scan files for the *Star* and *Wave* was updated offline, such that each scan line received an appropriate power command, as defined by the solution of the optimization problem (1). Figures 12 and 13 compare C_1 signals from the controlled and the open-loop layers of the parts for different scan directions. The *Star* (Fig. 12) test showed a reduction in 2-norm errors for each scan path: 28.0% and 24.6%, respectively. Similarly, the results from the *Wave* (Fig. 13) test showed a reduction of 25.1%, 25.5%, and 14.0% for each scan direction, demonstrating the efficacy of optimized power profiles. The geometry-dependent behavior of C_1 in corners and thin sections of the *Star* and *Wave* was visibly reduced in the controlled layers.

To assess the reduction of the geometry-related variation, the C_1 signal was filtered with the filter F (as in Fig. 8) due to high levels of variance. Once the filtered signal $F(C_1)$ was obtained, the standard deviation of $F(C_1)$, $\sigma(F(C_1))$ (commonly defined), was used to quantify the range of signal change. Figure 14 shows the $\sigma(F(C_1))$ for 20 layers of the controlled *Star* and *Wave* and compares it with the corresponding open-loop data. It is evident that, for both geometries, variation in the C_1 signal was reduced, with consistently lower values of $\sigma(F(C_1))$. The reduction of in-layer geometry-related variation in C_1 was approximately 50%. Thus, the model-based feedforward control was successful in regulating the undesirable melt pool behavior, and the control approach was experimentally validated.

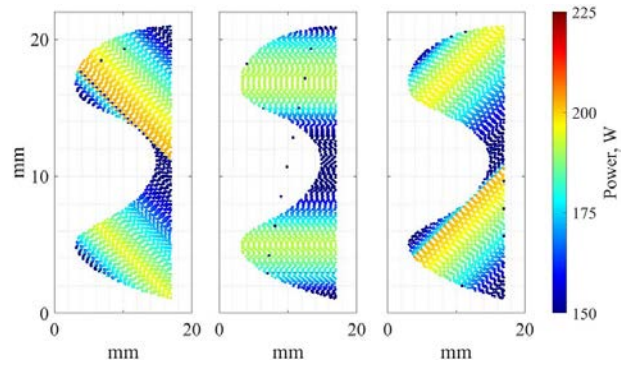

Fig. 11 Optimal power profiles for the *Wave* layer geometry for 3 different scanning raster angles

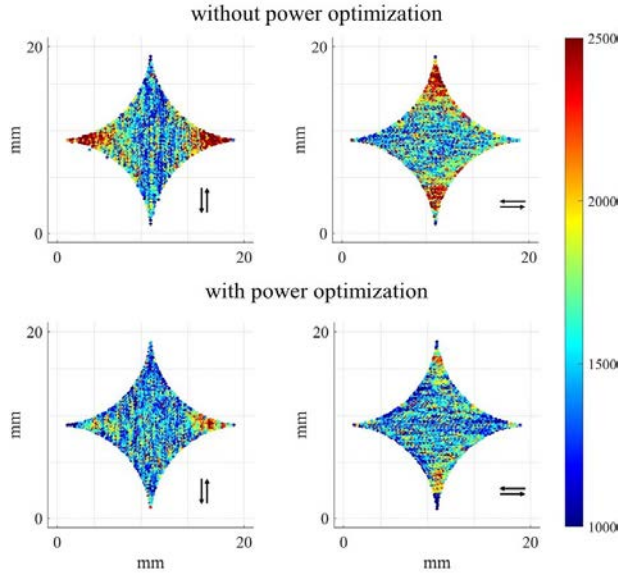

Fig. 12 C_1 signature with and without laser power optimization, *Star* case. Scan direction is indicated by arrows. Representative layers shown. In-layer variation of C_1 is decreased with model-based power control, and signal is closer to the setpoint of 1500, especially in the sharp corners. The reductions in 2-norm errors with respect to C_{ref} for each scan pattern are 28.0% and 24.6%, respectively.

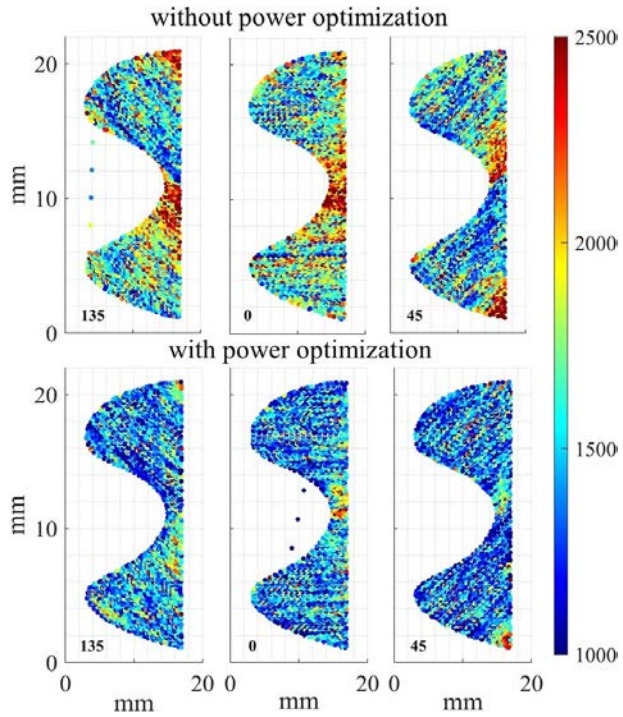

Fig. 13 A comparison between C_1 coaxial signature, with and without laser power optimization, in *Wave* case. Laser scan direction is indicated by angle value in degrees. Representative layers shown. In-layer variation of C_1 is decreased with model-based laser power control, and it is closer to setpoint of 1500, especially in the narrow section, and in the corners. The reductions in 2-norm errors with respect to C_{ref} for each scan pattern are 25.1%, 25.5%, and 14.0%, respectively.

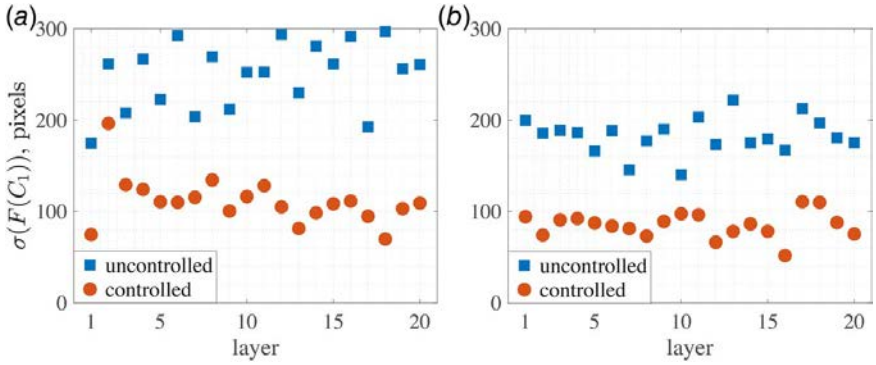

Fig. 14 A comparison between C_1 coaxial signature for the controlled and uncontrolled cases, for (*a*) *Star* and (*b*) *Wave* parts. Signal variation within a layer is reduced approximately two-fold.

6 Conclusion

In this letter, the behavior of the melt pool characteristics (such as the area of the melt pool footprint) was shown to depend on the geometry of the layer scan pattern. It was demonstrated that the footprint exponentially increases in size in the areas of a part where scan lengths shorten, e.g., in corners or narrow sections. The existence of such exponential behavior was observed on different parts and scan geometries, including the ones with non-straight edges. To capture this behavior, the empirical model, which incorporates variable laser power, was developed and experimentally validated. This model further enabled the application of a line-by-line model-based feedforward controller to regulate the footprint area. To reduce the signal deviations, optimal laser power profiles were calculated given the empirical model. These power profiles were then evaluated experimentally, for different geometries. The experimental evaluation of the proposed model-based feedforward control scheme demonstrated that such an approach reduces the geometry-induced changes in footprint area two-fold as compared to the open-loop operation.

Acknowledgment

This work was supported by NSF CMMI Award #2222250.

Conflict of Interest

There are no conflicts of interest.

Data Availability Statement

The datasets generated and supporting the findings of this article are obtainable from the corresponding author upon reasonable request.

References

[1] Zhang, B., Li, Y., and Bai, Q., 2017, "Defect Formation Mechanisms in Selective Laser Melting: A Review," Chin. J. Mech. Eng., **30**(3), pp. 515–527.
[2] Wang, D., Yang, Y., Yi, Z., and Su, X., 2013, "Research on the Fabricating Quality Optimization of the Overhanging Surface in SLM Process," Int. J. Adv. Manuf. Technol., **65**(9–12), pp. 1471–1484.
[3] Fox, J. C., Moylan, S. P., and Lane, B. M., 2016, "Effect of Process Parameters on the Surface Roughness of Overhanging Structures in Laser Powder Bed Fusion Additive Manufacturing," Procedia Cirp, **45**, pp. 131–134.
[4] King, W. E., Anderson, A. T., Ferencz, R. M., Hodge, N. E., Kamath, C., Khairallah, S. A., and Rubenchik, A. M., 2015, "Laser Powder Bed Fusion Additive Manufacturing of Metals: Physics, Computational, and Materials Challenges," Appl. Phys. Rev., **2**(4), p. 041304.
[5] Kruth, J.-P., Mercelis, P., Van Vaerenbergh, J., and Craeghs, T., 2007, "Feedback Control of Selective Laser Melting," Proceedings of the 3rd International Conference on Advanced Research in Virtual and Rapid Prototyping, Leiria, Portugal, Sept. 24–29, Taylor & Francis Ltd, pp. 521–527.
[6] Renken, V., Freyberg, A. V., Schünemann, K., Pastors, F., and Fischer, A., 2019, "In-Process Closed-Loop Control for Stabilising the Melt Pool Temperature in Selective Laser Melting," Prog. Addit. Manuf., **4**(4), pp. 411–421.
[7] Craeghs, T., Clijsters, S., Yasa, E., Bechmann, F., Berumen, S., and Kruth, J.-P., 2011, "Determination of Geometrical Factors in Layerwise Laser Melting Using Optical Process Monitoring," Opt. Lasers Eng., **49**(12), pp. 1440–1446.
[8] Vasileska, E., Demir, A. G., Colosimo, B. M., and Previtali, B., 2020, "Layer-Wise Control of Selective Laser Melting by Means of Inline Melt Pool Area Measurements," J. Laser Appl., **32**(2), p. 022057.
[9] Shkoruta, A., Mishra, S., and Rock, S. J., 2021, "Real-Time Image-Based Feedback Control of Laser Powder Bed Fusion," ASME Lett. Dyn. Syst. Control, **2**(2), p. 021001.
[10] Shkoruta, A., Caynoski, W., Mishra, S., and Rock, S., 2019, "Iterative Learning Control for Power Profile Shaping in Selective Laser Melting," IEEE International Conference on Automation Science and Engineering, Vancouver, BC, Canada, Aug. 22–26, pp. 655–660.
[11] Yeung, H., Lane, B., and Fox, J., 2019, "Part Geometry and Conduction-Based Laser Power Control for Powder Bed Fusion Additive Manufacturing," Addit. Manuf., **30**, p. 100844.
[12] Yeung, H., and Lane, B., 2020, "A Residual Heat Compensation Based Scan Strategy for Powder Bed Fusion Additive Manufacturing," Manuf. Lett., **25**, pp. 56–59.
[13] Yeung, H., Yang, Z., and Yan, L., 2020, "A Meltpool Prediction Based Scan Strategy for Powder Bed Fusion Additive Manufacturing," Addit. Manuf., **35**, p. 101383.
[14] Ren, Y., and Wang, Q., 2021, "Gaussian-Process Based Modeling and Optimal Control of Melt-Pool Geometry in Laser Powder Bed Fusion," J. Intell. Manuf., **33**(8), pp. 2239–2256.
[15] Wang, X., Lough, C. S., Bristow, D. A., Landers, R. G., and Kinzel, E. C., 2020, "A Layer-to-Layer Control-Oriented Model for Selective Laser Melting," 2020 American Control Conference (ACC), Denver, CO, July 1–3, IEEE, pp. 481–486.
[16] Yang, Y., Knol, M., van Keulen, F., and Ayas, C., 2018, "A Semi-Analytical Thermal Modelling Approach for Selective Laser Melting," Addit. Manuf., **21**, pp. 284–297.
[17] Wang, Q., Michaleris, P. P., Nassar, A. R., Irwin, J. E., Ren, Y., and Stutzman, C. B., 2020, "Model-Based Feedforward Control of Laser Powder Bed Fusion Additive Manufacturing," Addit. Manuf., **31**, p. 100985.
[18] America Makes, "4039 Development & Demonstration of Open-Source Protocols for Powder Bed Fusion AM." https://www.americamakes.us/projects/4039-development-demonstration-open-source-protocols-powder-bed-fusion-additive-manufacturing-pbfam/, Accessed July 2, 2023.
[19] Grantham, S., Lane, B., Neira, J., Mekhontsev, S., Vlasea, M., and Hanssen, L., 2016, "Optical Design and Initial Results From NIST's AMMT/TEMPS Facility," Laser 3D Manufacturing III, San Fransisco, CA, Feb. 13–18, Vol. 9738, SPIE, pp. 91–99.
[20] Gökhan Demir, A., De Giorgi, C., and Previtali, B., 2018, "Design and Implementation of a Multisensor Coaxial Monitoring System with Correction Strategies for Selective Laser Melting of a Maraging Steel," ASME J. Manuf. Sci. Eng., **140**(4), p. 041003.